

Mechanical injuries of neurons induce tau mislocalization to dendritic spines and tau-dependent synaptic dysfunction

Nicholas J. Braun^a, Katherine R. Yao^b, Patrick W. Alford^{a,1,2}, and Dezhi Liao^{b,1,2}

^aDepartment of Biomedical Engineering, University of Minnesota, Minneapolis, MN 55455; and ^bDepartment of Neuroscience, University of Minnesota, Minneapolis, MN 55455

Edited by Richard L. Huganir, Johns Hopkins University School of Medicine, Baltimore, MD, and approved September 26, 2020 (received for review May 6, 2020)

Chronic traumatic encephalopathy (CTE) is associated with repeated traumatic brain injuries (TBI) and is characterized by cognitive decline and the presence of neurofibrillary tangles (NFTs) of the protein tau in patients' brains. Here we provide direct evidence that cell-scale mechanical deformation can elicit tau abnormalities and synaptic deficits in neurons. Using computational modeling, we find that the early pathological loci of NFTs in CTE brains are regions of high deformation during injury. The mechanical energy associated with high-strain rate deformation alone can induce tau mislocalization to dendritic spines and synaptic deficits in cultured rat hippocampal neurons. These cellular changes are mediated by tau hyperphosphorylation and can be reversed through inhibition of GSK3 β and CDK5 or genetic deletion of tau. Together, these findings identify a mechanistic pathway that directly relates mechanical deformation of neurons to tau-mediated synaptic impairments and provide a possibly exploitable therapeutic pathway to combat CTE.

traumatic brain injuries | dendritic spines | tau | chronic traumatic encephalopathy | synaptic deficits

Traumatic brain injury (TBI) is a critical public health concern largely due to associated long-term neurological deficits. In the United States, there are 1.6 to 3.8 million TBIs annually, and ~5.3 million Americans are living with a disability stemming from a TBI (1–3). A TBI is commonly caused by a fall, being struck by an object, or an automobile crash, but recent interest in TBI stems from observations of long-term neurodegenerative pathologies in former athletes and military veterans who sustained mild TBIs during their careers. Evidence of chronic traumatic encephalopathy (CTE) in autopsies of former professional athletes suggests a link between long-term repetitive TBI and memory deficits, behavioral changes, and neurodegenerative symptoms (4–8). Service members who survive a TBI are significantly more likely to develop CTE, Alzheimer's disease (AD), and frontotemporal dementia (FTD) (9–14), all of which are neurodegenerative diseases classified as tauopathies, which are characterized by deposits of pathological forms of the protein tau in the brains of the patients. Although CTE brains contain tau pathologies that are similar to those in AD and FTD, no published studies have provided direct experimental evidence linking mechanical deformation of neurons to tau-mediated functional deficits at a cellular level.

Tau is a microtubule-associated protein that is highly concentrated in the axons of healthy central nervous system neurons (15). Tau's functions include uniformly spacing parallel microtubules and preventing microtubule depolymerization (16, 17). In some tauopathy models, disease-state tau has been shown to interfere with molecular pathways in axonal transport and the release of synaptic vesicles and mislocalize to the neuronal soma, dendrites, and dendritic spines, resulting in synaptic impairment (18–24). Posttranslational modifications of soluble tau, including phosphorylation by proline-directed kinases (20–23), phosphorylation triggered by unfolded protein response (25), cleavage by

capsase-2 (26), and acetylation by CBP (27, 28), have been associated with memory deficits, synaptic dysfunction, and the mislocalization of tau to dendritic spines. This mislocalization of tau has been shown to mediate synaptic dysfunction in the neuronal models of both AD and FTDP-17 (20, 21, 23). Shared tau pathology and cognitive deficits observed in CTE and other tauopathies encouraged us to elucidate the consequences of TBI on the cellular scale.

Here we report an in vitro tauopathy model of TBI that links neuron-scale mechanical deformations to tau abnormalities and synaptic deficits in cultured hippocampal rat neurons. Using our in vitro TBI system, we found that high-strain rate mechanical deformation alone can induce tau mislocalization and tau phosphorylation-dependent synaptic dysfunction. The tau abnormalities and synaptic deficits were shown to be preventable by inhibition of CDK5 and GSK3 β , which are two widely studied kinases that phosphorylate tau. They can also be ameliorated by genetic deletion of tau. The present study provides experimental evidence that directly links mechanical injury to tau-mediated synaptic deficits. The rescuing of synaptic impairments by the inhibition of tau mislocalization to dendritic spines may represent a therapeutic strategy to prevent CTE and other neurodegenerative diseases in patients afflicted with TBI.

Significance

Athletes and soldiers exposed to repeated traumatic brain injuries have increased risk of developing chronic traumatic encephalopathy (CTE), which is a neurodegenerative disease characterized by tangled deposits of the protein tau in the brain and loss of cognitive function. This study provides the first experimental evidence showing that mechanical stretching of neurons induces tau to be mislocalized to dendritic spines where it causes synaptic dysfunction. This cross-disciplinary study utilizes computational modeling, imaging, and electrophysiology to unravel a cellular framework for how tau phosphorylation mediates trauma-induced synaptic dysfunction, highlighting the essential role of tau in functional deficits caused by traumatic brain injury.

Author contributions: N.J.B., P.W.A., and D.L. designed research; N.J.B., K.R.Y., P.W.A., and D.L. performed research; D.L. contributed new reagents/analytic tools; N.J.B., K.R.Y., P.W.A., and D.L. analyzed data; and N.J.B., P.W.A., and D.L. wrote the paper.

The authors declare no competing interest.

This article is a PNAS Direct Submission.

Published under the PNAS license.

¹P.W.A. and D.L. contributed equally to this work.

²To whom correspondence may be addressed. Email: pwalford@umn.edu or liaox020@umn.edu.

This article contains supporting information online at <https://www.pnas.org/lookup/suppl/doi:10.1073/pnas.2008306117/-DCSupplemental>.

First published November 2, 2020.

Results

High Strains in Brain Tissue Are Correlated with CTE Pathological Hallmarks. In tauopathies, phosphorylated tau (p-tau) accumulates into dense aggregates called neurofibrillary tangles (NFTs) (29). While NFTs are a common pathophysiological hallmark of tauopathies, their distribution throughout the brain differs between diseases. In CTE, p-tau NFTs primarily aggregate in superficial cortical layers, sulci, and perivascular regions (Fig. 1A) (7–9, 30–33). This is in contrast to other tauopathies like AD, in which NFT localization is more uniformly distributed in the deeper-lying cortical layers and not concentrated in sulcal depths or perivascular regions (33). To determine the relationship between mechanical deformation of the brain and the occurrence of CTE hallmarks, we created 2D, quasi-static, finite-element models of a sulcus and microvessel during impact injury. First, depression of a rigid impactor on a geometrically symmetric sulcus was simulated, mimicking contact between the brain and skull during TBI. During impact, the model indicated that the first principal strains were largest in the sulcal depths and that the largest strains were positive, meaning the tissue was being stretched (Fig. 1B–E). These results were consistent with previous whole-brain models (34). Although the magnitude of the strain varied with sulcus geometry, the peak strain consistently occurred in the depth of the sulcus (Fig. 1D and E and *SI Appendix, Fig. S1*). Next, depression of brain tissue surrounding a pressurized microvessel was simulated. This model demonstrated that the largest strains occur immediately around the vessel and that this effect is exaggerated in smaller vessels and when the vessel modulus is stiff compared to the brain modulus (Fig. 1F–H and *SI Appendix, Fig. S2*). These results suggest a correlation between mechanical deformation and tau pathology in CTE patients and that mechanical stretching can be used to simulate the effects of TBI in brain tissue.

Mechanical Stretching of Cultured Neurons Induces Tau Mislocalization to Dendritic Spines and Associated Synaptic Deficits. To study the effect of brain deformation on tauopathy, a custom-designed

stretcher (35, 36) was used to apply high-strain rate deformation to primary hippocampal neurons seeded on an elastic membrane (Fig. 2A and B). Previous studies have shown that tau mislocalizes to dendritic spines in models of neurodegenerative disease (20–23), so we sought to track its localization in neurons following stretch-induced injury using neurons that were cotransfected with DsRed and WT-tau-GFP plasmids to allow for identification of dendritic spines and tau (Fig. 2C and D). In unstretched controls, ~20% of dendritic spines had a detectable tau presence. In neurons exposed to a single stretch of 20% strain (ϵ), at a strain rate ($\dot{\epsilon}$) of 1,000%/s, we found significant tau mislocalization to dendritic spines 24 h poststretch (Fig. 2D and E), with no significant decrease in dendritic spine density (Fig. 2F), demonstrating that stretch injury can drive tau pathology in vitro. These injury parameters were comparable to strains and strain rates gathered from in vivo models of TBI (37). Tau mislocalization to dendritic spines was further verified using immunocytochemistry, which showed that both transfected WT-Tau-GFP and endogenous tau were increased in mushroom-like structures that are colocalized with/attached to Synaptophysin, a synaptic marker, after a mechanical injury to neurons (*SI Appendix, Figs. S3 and S4*). Additionally (in this experiment and all following tau mislocalization experiments), no relationship was seen between observed tau mislocalization and the ratio of DsRed:GFP fluorescent intensity, indicating that variations in fluorescent protein expression levels do not explain tau mislocalization (*SI Appendix, Fig. S5*). This tau mislocalization is consistent with that seen in other tauopathy models, such as FTDP-17 and AD (20–23), further supporting a role of tau mislocalization in multiple neurodegenerative diseases (24).

In FTDP-17 and AD, tau mislocalization corresponds with synaptic deficits (20–23), so next we aimed to investigate whether stretch-induced tau mislocalization caused similar loss of synaptic function. We used whole-cell patch clamp to record miniature excitatory postsynaptic currents (mEPSCs) whose amplitudes and frequencies can be quantified as a proxy for synaptic health or functionality (Fig. 2G) (20–23). Twenty-four hours poststretch ($\epsilon = 20\%$, $\dot{\epsilon} = 1,000\%/s$) we observed a significant decrease in mEPSC amplitude (Fig. 2H and I), likely indicating decreased

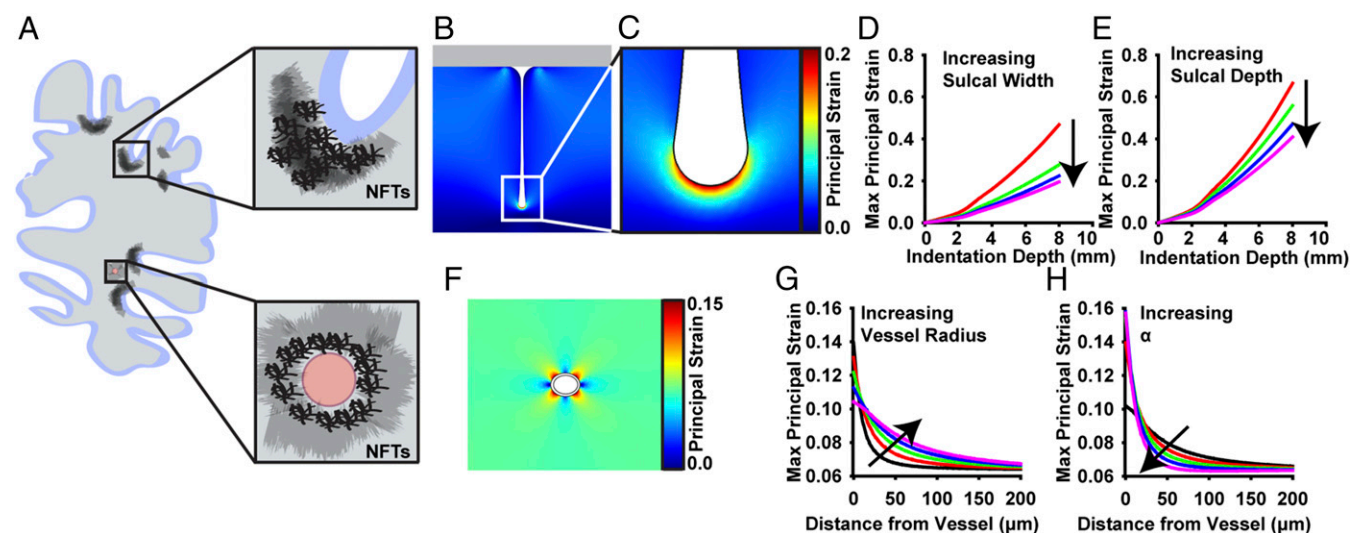


Fig. 1. CTE-associated p-tau NFTs accumulate in regions of the brain that undergo the greatest mechanical deformation during TBI. (A) NFTs accumulate in the sulcal depths and perivascular regions of the brain in CTE patients (7). (B and C) Two-dimensional quasi-static, finite element model of a single sulcus during impact injury. First principal strain is at a maximum in the deepest part of the sulcal depth. (D and E) Parametric studies of the effect of brain geometry on maximum principal strain during impact in the sulcus model. (D) Effect of sulcal width on maximum first principal strain (width = 5, 10, 15, and 20 mm). (E) Effect of sulcal depth on maximum first principal strain (depth = 50, 60, 70, and 80 mm). (F) Two-dimensional quasi-static, finite element model of a perivascular region surrounding a single pressurized blood vessel. First principal strain is at a maximum nearest the vessel. (G and H) Parametric studies of the effect of vessel geometry and material properties on principal strain during brain deformation. (G) Effect of vessel outer radius on spatial strains (radius = 30, 40, 50, 60, and 70 mm). (H) Effect of vessel modulus on spatial strains, where $E_{\text{vessel}} = \alpha E_{\text{brain}}$ ($\alpha = 3, 9, 21, 41$, and 81).

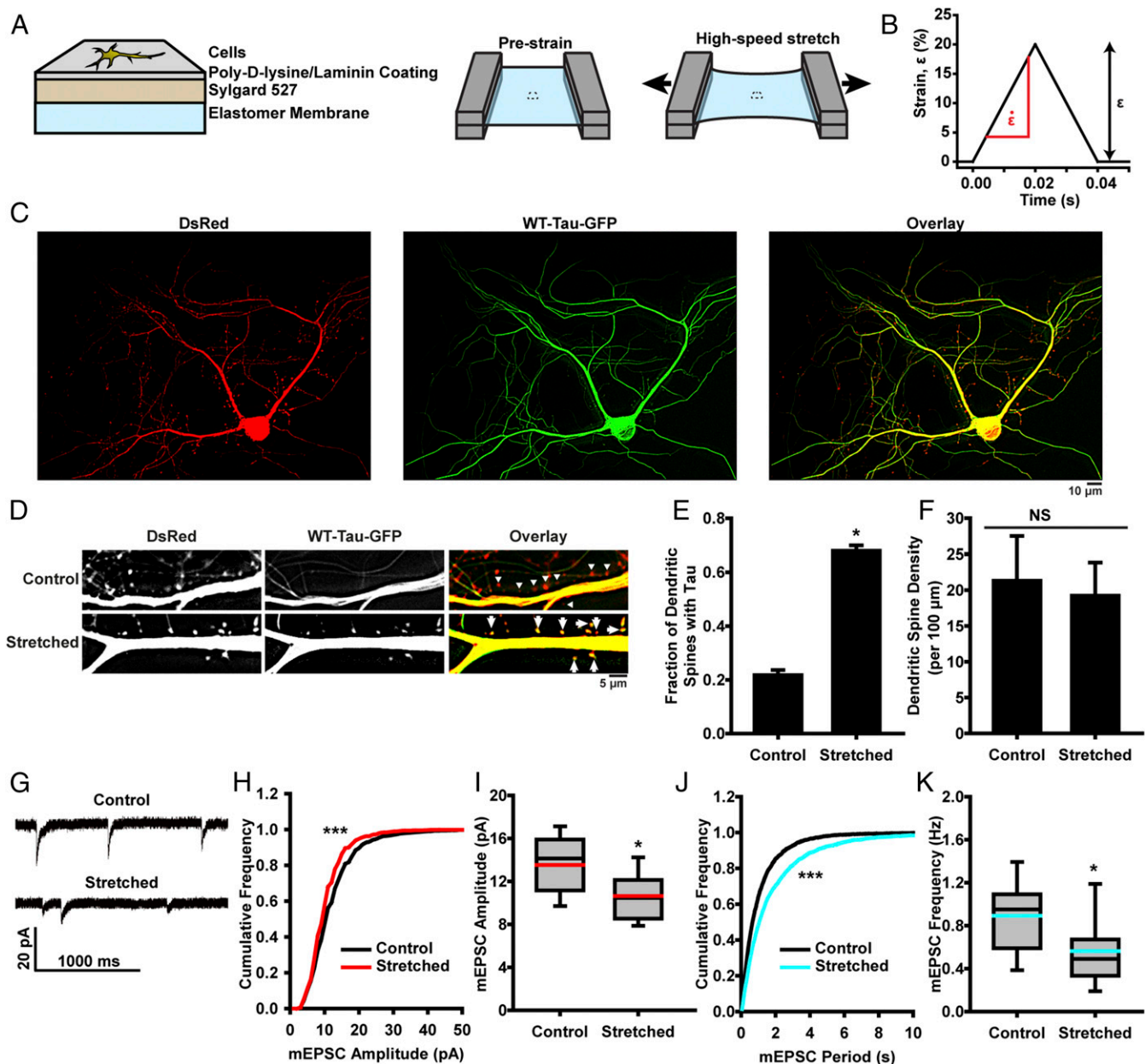


Fig. 2. Neurons exposed to high-strain rate deformation exhibit tau abnormalities and synaptic functional deficits. (A) Schematic representation of in vitro TBI system construct fabrication and stretching. (B) Prescribed temporal wave form for a stretch of 20% strain (ϵ) and 1,000%/s strain rate ($\dot{\epsilon}$). (C) Representative images of cultured rat hippocampal neurons transfected with DsRed (Left) and WT-Tau-GFP (Center). Images overlaid to assess tau mislocalization (Right). (D) Representative images of tau mislocalization in to dendritic spines in control and stretched neurons. Arrows denote spines with tau, and triangles indicate spines without tau. (E) Quantification of tau mislocalization, measured as fraction of spines with tau present, in unstretched control and stretched neurons (mean \pm SD). Spines/images: control, 669/23; stretched, 524/7. (F) Spine density in unstretched control and stretched neurons (mean \pm SD). (G) Representative mEPSCs recorded from unstretched control and stretched neurons. (H) Cumulative frequency of mEPSC amplitude (black line, median; red line, mean; box, 25 to 75%; whisker, 10 to 90%). K-S test: $D/D_{crit} = 4.31$, $\alpha = 0.05$, bins = 1 pA. (I) Quantification of mEPSC amplitudes (black line, median; red line, mean; box, 25 to 75%; whisker, 10 to 90%). K-S test: $D/D_{crit} = 5.48$, $\alpha = 0.05$, bins = 50 ms. (J) Cumulative frequency of mEPSC peak-to-peak period (black line, median; teal line, mean; box, 25 to 75%; whisker, 10 to 90%). K-S test: $D/D_{crit} = 5.48$, $\alpha = 0.05$, bins = 50 ms. (K) Quantification of mEPSC frequency (black line, median; teal line, mean; box, 25 to 75%; whisker, 10 to 90%). Cells/mEPSCs: control, 18/4,360; stretched, 23/3,139. In all plots, * $P < 0.05$, *** $P < 0.001$ compared to control, and NS is not significant.

AMPA presence in the spines of postsynaptic neurons (38–40). We also observed decreased mEPSC frequency (Fig. 2 J and K), suggesting a decreased release rate of neurotransmitter vesicles in presynaptic terminals (41). Tau mislocalization was found to precede electrophysiological changes in the hours immediately following stretch injury (SI Appendix, Fig. S6). Taken together, these results suggest that stretch alone can induce presynaptic and postsynaptic functional deficiencies.

Tau Mislocalization Depends on Injury Dynamics. Although the exact etiology of mechanically induced tauopathy is not known, CTE is typically associated with repeated mild head injuries, not a single trauma. Thus, we sought to characterize the relationship between injury strain rate, strain magnitude, and tau mislocalization. In neurons stretched to $\epsilon = 20\%$ strain at varying rates of $\dot{\epsilon} = 1, 10, 100$, and 1,000%/s, the highest strain rate stretching induced tau mislocalization, consistent with our earlier results, but at

lower strain rates, we observed no significant mislocalization, when compared to controls (Fig. 3 A–C). In neurons stretched with varying strain ($\epsilon = 12, 5, 10$, and 20%) at a high-strain rate ($\dot{\epsilon} = 1,000\%/s$), strains below 5% did not induce significant tau mislocalization, while in cells stretched 5 to 20% , mislocalization increased monotonically with increasing strain magnitude (Fig. 3 D–F). These data demonstrate the direct relationship between the dynamics of mechanical stimulus and severity of tauopathic consequences.

Brain tissue and neurons have viscoelastic material properties (42–46). The dependence of tau mislocalization on both strain and strain rate in our experiments suggests that this viscoelasticity mediates trauma-induced tauopathy. We modeled the neuron as a standard viscoelastic solid (Fig. 3 G), with material properties based on previously published studies (46) and calculated the work done on the cell during stretching. When the work was compared to the measured tau mislocalization, we found that below 1 kJ/m^3 , mislocalization did not occur, but above that threshold value, mislocalization increased monotonically with increasing work (Fig. 3 H). This result suggests that tau mislocalization is directly related to the mechanical energy added to the neuron during trauma.

To simulate repeated trauma, we applied periodic stretches of $\epsilon = 2\%$, $\dot{\epsilon} = 1,000\%/s$, with 1 -s intervals between stretches.

Consistent with our previous results, a single stretch did not induce of tau mislocalization. Similarly, there was no significant mislocalization following five repetitions. However, following 10 and 20 repetitions at small strain, we observed tau mislocalization similar to that seen in neurons exposed to a single high-strain rate stretch (Fig. 4 A–C). We applied our viscoelastic model to the repeated stretch conditions and found that mislocalization correlated with the cumulative work of the stretches (Fig. 4 D). These data suggest that our in vitro and in silico models are able to capture some aspects of the cumulative consequences of repeated mild TBI.

Tau Is Required for Stretch-Induced Synaptic Deficits. To demonstrate that tau is required to give rise to functional deficits, we employed a Tau-KO mouse model (from Jackson Laboratory; B6.129 \times 1-Mapt^{tm1Hnd}/J). In 3-wk-old neurons harvested from TgNg control mice, a stretch injury of $\epsilon = 20\%$, $\dot{\epsilon} = 1,000\%/s$ led to a decrease in both the amplitude and frequency of mEPSCs (Fig. 5 A–F), consistent with our findings in rat neurons. In 3-wk-old neurons from Tau-KO mice, the average amplitude and frequency of mEPSCs were not statistically different from unstretched Tau-KO neurons, implying that tau pathology is necessary for functional synaptic deficits after a mechanical injury (Fig. 5 G–L). However, when comparing the effects of

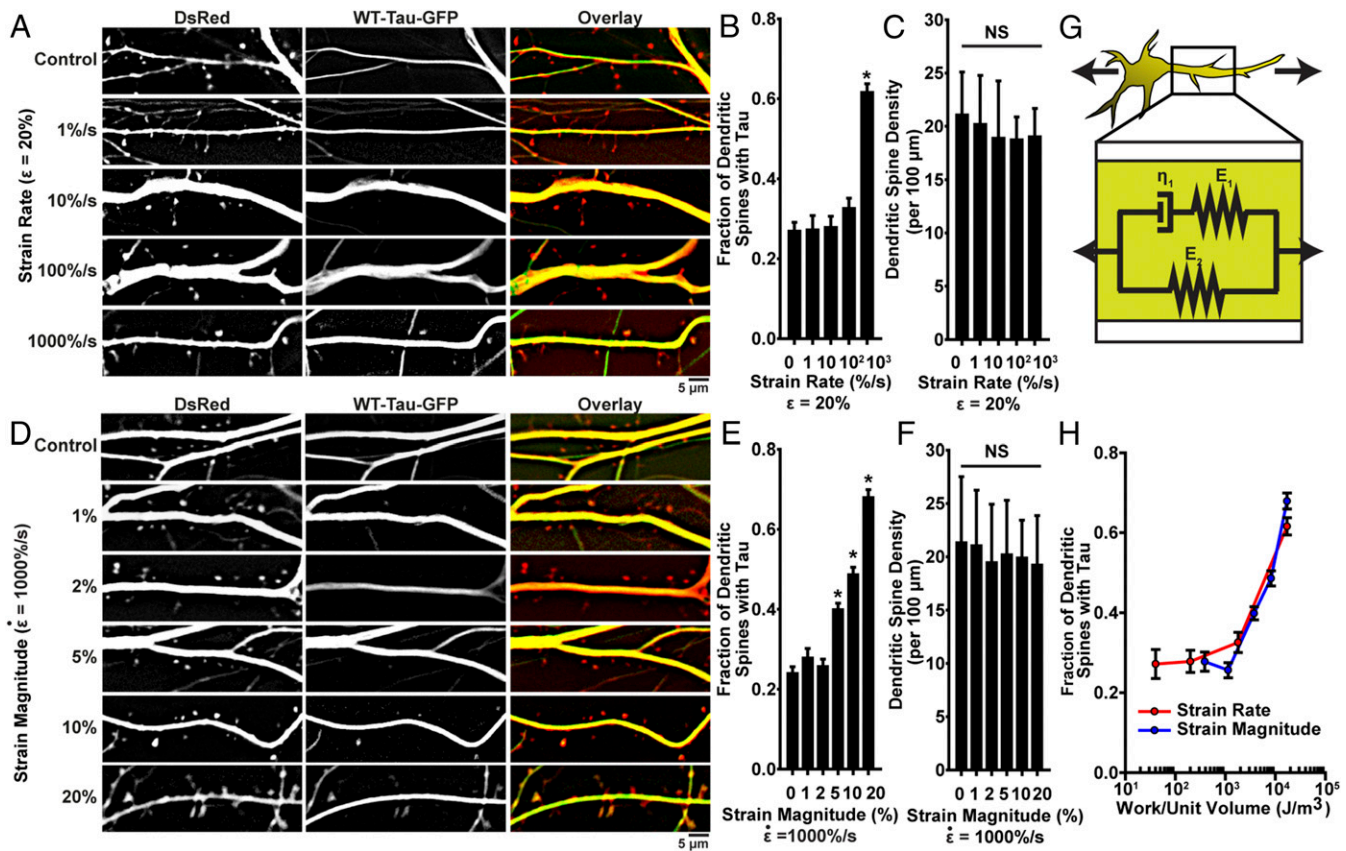


Fig. 3. Tau mislocalization driven by mechanical injury is dependent on injury dynamics. (A) Representative images of tau mislocalization in neurons stretched to $\epsilon = 20\%$ strain with varying strain rates ($\dot{\epsilon} = 1, 10, 100$, and $1,000\%/s$). (B) Tau mislocalization, measured as fraction of spines with tau present, as an effect of strain rate. Spines/images: control, 402/10; $1\%/s$, 351/10; $10\%/s$, 259/7; $100\%/s$, 344/9; $1,000\%/s$, 505/8. (C) Total spine density as an effect of strain rate. (D) Representative tau mislocalization in neurons stretched with varying strains ($\epsilon = 1, 2, 5, 10$, and 20%) at a strain rate of $\dot{\epsilon} = 1,000\%/s$. (E) Tau mislocalization, measured as fraction of spines with tau present, as an effect of strain magnitude. Spines/images: control, 669/23; 1% , 346/10; 2% , 527/11; 5% , 866/16; 10% , 702/16; 20% , 542/7. (F) Spine density as an effect of strain magnitude. (G) Schematic representation of the standard viscoelastic solid used to model neurons during stretch. (H) Model-predicted mechanical work during stretching compared with experimentally measured tau mislocalization for all conditions measured in A–F (red, varying strain rate [A–C]; blue, varying strain magnitude [D–F]). In all plots, $*P < 0.05$ compared to control, and NS is not significant.

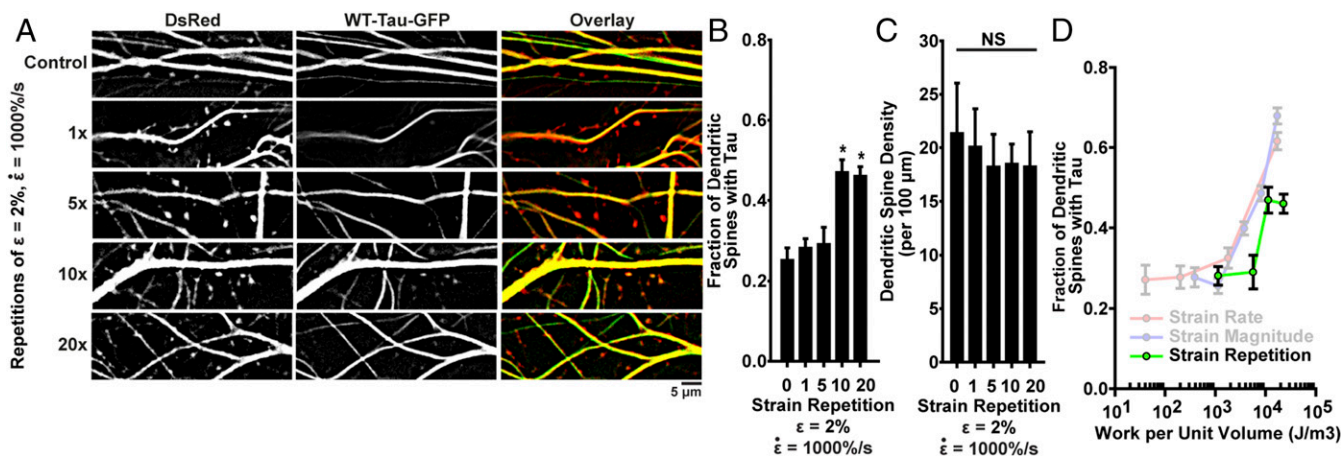


Fig. 4. Repeated mild injuries induce tau mislocalization similar to a single severe injury. (A) Representative images of tau mislocalization in neurons exposed to periodic stretches of $\epsilon = 2\%$, $\dot{\epsilon} = 1,000\%/s$. (B) Tau mislocalization, measured as fraction of spines with tau present, as an effect of number of stretches. Spines/images: control, 299/9; 1x, 384/6; 5x, 277/6; 10x, 241/5; 20x, 437/5. (C) Spine density as an effect of number of stretches. (D) Additive work predicted by the viscoelastic model for repeated stretches compared with experimentally measured tau mislocalization. In all plots, mean \pm SD, * $P < 0.05$ compared to control, and NS is not significant.

mechanical injury on mEPSC characteristics in TgNg and Tau-KO neurons as a percentage difference relative to unstretched controls, it is apparent that postsynaptic processes are more affected by tau than presynaptic processes in our injury model (Fig. 5 *M* and *N*). Our results show an mEPSC amplitude decrease of 17.35% in TgNg neurons compared to a small 1.02% decrease in Tau-KO neurons, indicating that postsynaptic impairment is largely tau-dependent. In contrast, mEPSC frequency was decreased by 25.78% in TgNg neurons compared to 12.58% in Tau-KO neurons, suggesting that factors other than tau contribute to a significant portion of the presynaptic impairment seen after mechanical injury.

Stretch-Induced Tauopathy Is Mediated by Tau Hyperphosphorylation. CTE-associated NFTs are composed of hyperphosphorylated tau (31). Thus, we next examined the role of tau hyperphosphorylation on tau mislocalization in our in vitro injury model. Neurons were transfected with AP tau-GFP (20), in which 14 serines(S)/threonines(T) are replaced with alanines, disallowing proline-directed phosphorylation of these residues. Following a stretch of $\epsilon = 20\%$, $\dot{\epsilon} = 1,000\%/s$, there was minimal tau presence in dendritic spines, indicating that tau must be hyperphosphorylated at some of the 14 S/T residues to mislocalize in our in vitro injury model (Fig. 6 *A–C*).

Next, the two main kinases responsible for hyperphosphorylating tau, GSK3 β and CDK5 (22, 23, 47, 48), were inhibited with CHIR99021, Roscovitine, or both, prior to stretch. Neurons treated with either inhibitor individually showed reduced tau mislocalization, and treatment with both inhibitors concurrently further reduced mislocalization, supporting the previous findings that tau mislocalization is phosphorylation-dependent (Fig. 6 *D–F*).

Finally, mEPSCs were measured in neurons treated with CHIR99021 and Roscovitine (Fig. 7 *A–L* and *SI Appendix, Fig. S7*). Treatment with either inhibitor individually yielded a partial recovery of mEPSC amplitude and frequency in cells exposed to stretch. Following treatment with both inhibitors, we observed full recovery on mEPSC amplitude and partial recovery of frequency (Fig. 7 *M* and *N*). These results suggest that tau mislocalization is the primary source of postsynaptic deficit in mechanically induced tauopathy and is a contributor to presynaptic dysfunction as well. These data further suggest that inhibition of tau hyperphosphorylation can act to preserve synaptic function following stretch injury (Fig. 7*O*).

Discussion

During TBI, the brain undergoes acute mechanical deformation at high strain rates, causing damage to neurons and glial cells (48–52). This mechanical injury initiates the cascade of neurotraumatic consequences that lead to the cognitive and behavioral symptoms seen in TBI patients. In tauopathies, cognitive defects are linked to the presence of tau lesions. Unlike AD brains, in which tau lesions start at the midbrain, the earliest pathological lesions of CTE brains are deposits of p-tau aggregates in sulcal depths and perivascular regions of the cortex (53). In our computational simulation studies, we observed that maximum principal strains occur in sulcal depths and perivascular regions, supporting a mechanistic link between high strain in brain tissues, subsequent tau pathology, and the earliest lesions of CTE.

Building on these simulation results, we modeled neuronal injury using high-strain rate stretching. Using this in vitro model of tauopathy in TBI, we have provided direct cellular evidence linking mechanical stretching to tau abnormalities. We found that tau mislocalization to dendritic spines can be induced by a variety of TBI simulations, including a single large mechanical injury or multiple repetitive injuries of lesser severity. Our viscoelastic model suggests that a key determinant of the severity of tauopathy is the mechanical energy added to the neuron during deformation. Previous studies have shown that mechanical forces can induce axonal focal swelling, akin to diffuse axonal injury observed in vivo (54, 55), and theoretical studies have suggested that the viscoelasticity of the tau protein mediates strain rate-dependent collapse of microtubules in focal swellings (56). Here we did not observe any focal swelling, but our results suggest that a similar viscoelastic mechanism plays a role in injury in subaxonal-collapse deformations. This mechanical energy model is important for understanding injury likelihood due to dynamic loads like those caused by blast waves experienced by soldiers (9), which often have complex pressure waveforms that may exacerbate injury (57, 58). In addition, this model could shed light on the biomechanical contribution from TBI that leads to development of AD, CTE, and other tauopathies.

Our studies demonstrate the essential roles of tau hyperphosphorylation and tau mislocalization to dendritic spines in mechanical injury-induced functional deficits in excitatory synaptic transmission. We have previously reported that tau mislocalization to dendritic spines is associated with postsynaptic dysfunctions in multiple models of neurodegenerative diseases

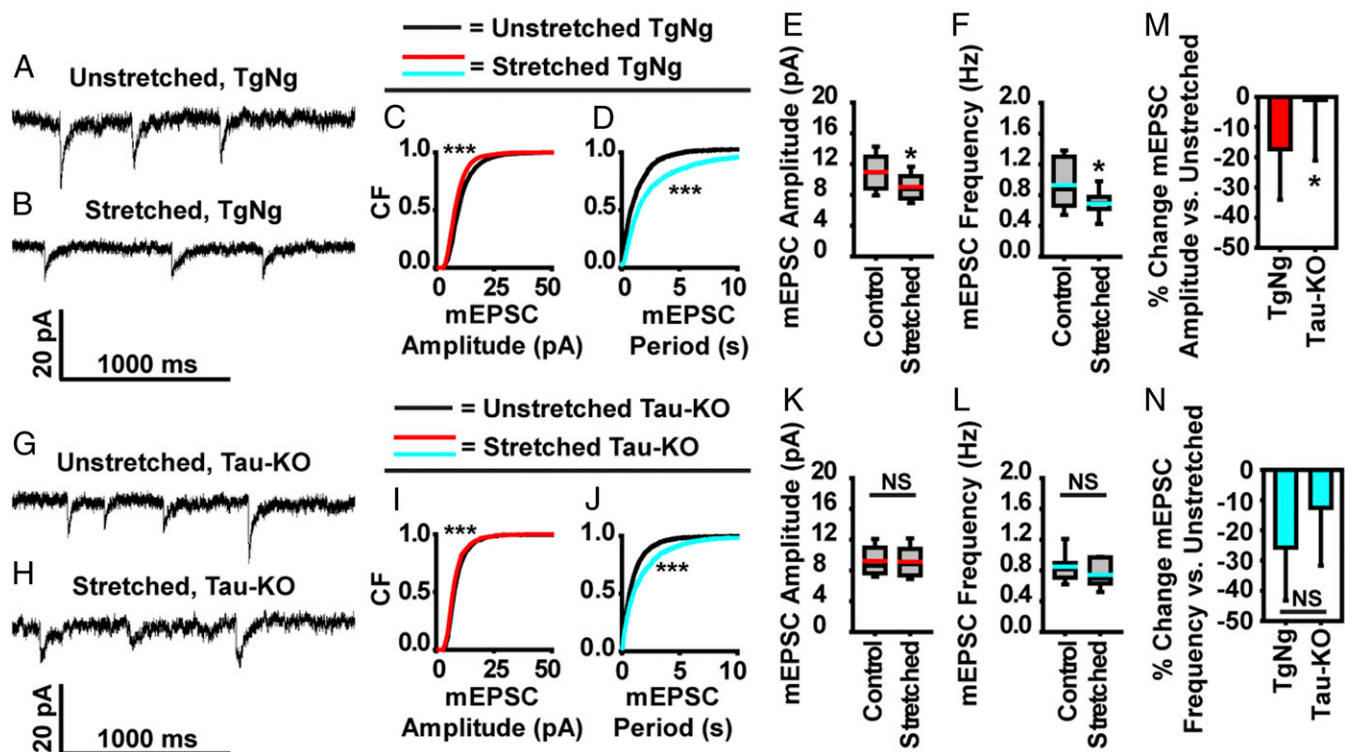


Fig. 5. Blockage of postsynaptic dysfunction following stretch injury and partial blockage of presynaptic dysfunction in tau knockout mice. (A and B) Representative mEPSC recordings from TgNg neurons that were left unstretched or were injured with a stretch. (C) Cumulative frequency of mEPSC amplitudes (black, unstretched control; red, stretched; bins, 1 pA). (D) Cumulative frequency of mEPSC peak-to-peak period (black, unstretched control; teal, stretched; bins, 50 ms). (E) Quantification of mEPSC amplitudes (black line, median; red line, mean; box, 25 to 75%; whisker, 10 to 90%). (F) mEPSC frequency (black line, median; teal, mean; box, 25 to 75%; whisker, 10 to 90%). (G and H) Representative mEPSC recordings from Tau-KO neurons that were left unstretched or were injured with a stretch. (I) Cumulative frequency of mEPSC amplitudes (black, unstretched control; red, stretched; bins, 1 pA). (J) Cumulative frequency of mEPSC peak-to-peak period (black, unstretched control; teal, stretched; bins, 50 ms). (K) Quantification of mEPSC amplitudes (black line, median; red line, mean; box, 25 to 75%; whisker, 10 to 90%). (L) mEPSC frequency (black line, median; teal, mean; box, 25 to 75%; whisker, 10 to 90%). (M) Percentage change in mEPSC amplitude of stretched TgNg neurons relative to unstretched TgNg neurons (left bar) is compared with that in stretched Tau-KO neurons relative to unstretched Tau-KO neurons (right bar). (N) Percentage change in mEPSC frequency of stretched TgNg neurons relative to unstretched TgNg neurons (left bar) is compared with that in stretched Tau-KO neurons relative to unstretched Tau-KO neurons (right bar). For cumulative frequency distribution plots, K-S tests were used to compare treated and/or stretched groups to unstretched-untreated controls. D/D_{crit} : C, 4.15; D, 5.74; I, 1.37; J, 1.70; $\alpha = 0.05$ for all. Cells/mEPSCs: TgNg-unstretched, 14/3,197; TgNg-stretched, 16/2,985; Tau-KO-unstretched, 11/1,150; Tau-KO-stretched, 11/1,007. In all plots, $*P < 0.05$, $***P < 0.001$ compared to control, and NS is not significant.

including AD (21) and FTDP-17 (20). Consistent with previous findings, here we found that the amplitudes of mEPSCs were decreased in neurons exposed to high-strain rate stretching, indicating that mechanical injuries can impair postsynaptic function by decreasing the number of AMPA receptors in dendritic spines. Mechanical stretching also decreased the frequency of mEPSCs, which may be a result of decreased releasing probability (p) and/or releasing sites (n) (59). We found no significant change in spine density, suggesting there was no change in number of synapses and thus no change in n. Therefore, this result suggests that mechanical injuries also impair the release of presynaptic vesicles, likely by disrupting tau-related axonal transport. Alternatively, the change in mEPSCs may be attributable solely to loss of AMPA receptors, as this change can reduce the number of detectable releasing sites (n) by decreasing the number of detectable active synapses and by increasing the number of silent synapses (60).

The signaling cascades upstream to and downstream from mechanical stretching-induced phosphorylation-dependent tau mislocalization to dendritic spines are not yet fully clarified. It has been hypothesized that during TBI, shearing force causes extensive axonal injury and detaches tau proteins from microtubules, which subsequently causes tau hyperphosphorylation

and neuronal impairment (61). The results here provide direct cellular evidence in support of this widely believed but not yet confirmed hypothesis. Our experiments highlight the importance of tau hyperphosphorylation in tau mislocalization (Fig. 6 A–C), and we were able to identify potential pathways that could be exploited to mitigate some of the neurodegenerative consequences of TBI. Inhibition of both GSK3 β and CDK5, two primary kinases that phosphorylate tau, reduced both the tauopathic and electrophysiological impairments of in vitro TBI.

Interestingly, mechanical injury-induced postsynaptic impairment is mostly blocked by genetic deletion of tau, as seen in our Tau-KO experiments. This was not true for presynaptic impairment, as a significant amount of presynaptic deficits remained in injured neurons with a genetic tau deletion (Fig. 5). The synaptic vesicle precursors, which provide most key presynaptic proteins, are transported along microtubule tracks by the kinesin-3 motors (62, 63). Mechanical stretching of axons could impair axonal transport by disrupting the organization of microtubules in as little as 2 min (64). The disruption of microtubules is believed to precede the detachment of tau proteins from microtubules and subsequent tau hyperphosphorylation (61). Therefore, it is likely that microtubule disruption caused by axonal injury may impair presynaptic function through tau-independent mechanisms as

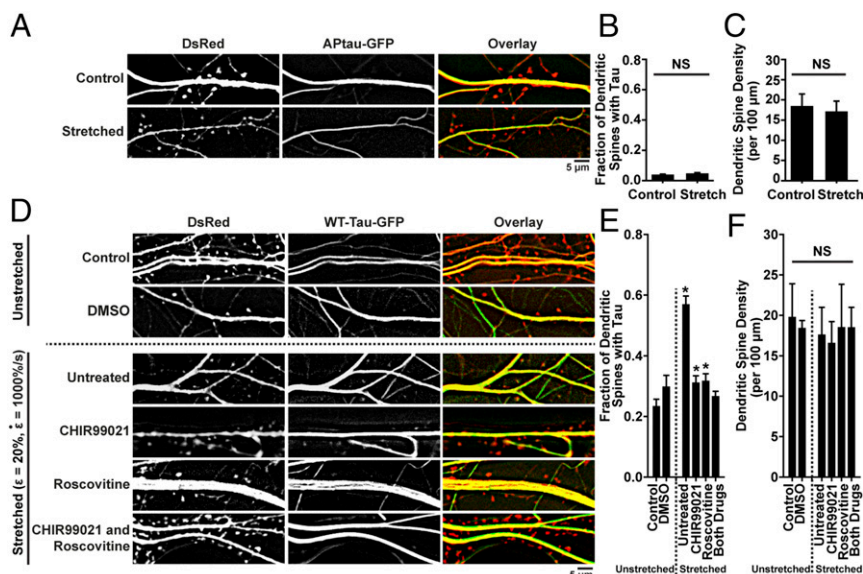


Fig. 6. Tau mislocalization is phosphorylation-dependent. (A) Representative images of tau mislocalization in control and stretched ($\epsilon = 20\%$, $\dot{\epsilon} = 1,000\%/s$) neurons transfected with DsRed and APTau-GFP, a form of tau that cannot be phosphorylated. (B) Quantification of tau mislocalization, measured as fraction of spines with tau present, in unstretched control and stretched neurons transfected with APTau-GFP. Spines/images: control, 548/13; stretched, 447/12. (C) Quantification of spine density in unstretched control and stretched neurons transfected with APTau-GFP. (D) Representative images of tau mislocalization in unstretched and stretched neurons ($\epsilon = 20\%$, $\dot{\epsilon} = 1,000\%/s$) untreated or treated with 500 nM CHIR99021 to inhibit GSK3 β , 500 nM Roscovitine to inhibit CDK5, or both. (E) Tau mislocalization as an effect of stretch, following GSK3 β and CDK5 inhibitor treatment. Spines/images: control, 289/9; DMSO, 195/6; untreated, 287/17; CHIR99021, 324/10; Roscovitine, 365/15; both drugs, 582/18. (F) Spine density as an effect of stretch, following GSK3 β and CDK5 inhibitor treatment. In all plots, mean \pm SD, * $P < 0.05$, compared to unstretched control, and NS is not significant.

experimentally shown in Fig. 5. In contrast, tau hyperphosphorylation is essential for aberrant accumulation of tau proteins in postsynaptic structures and subsequent postsynaptic dysfunction (20, 24). The blockage of most postsynaptic deficits in Tau-KO mice neurons shown in Fig. 5 is consistent with previous tau studies (24) and supports our hypothetical model in Fig. 7O.

In summary, our results clearly demonstrate that the rate and magnitude of brain deformation during TBI influence tau-mediated neural injuries, providing a plausible neurobiological explanation for the formation of tau deposits in sulcal depths and perivascular regions, the two pathological hallmarks of CTE. Mechanistically, we have provided a molecular framework (Fig. 7O), by which mechanical injuries lead to tau hyperphosphorylation, tau mislocalization, and tau-dependent impairment of excitatory synaptic functions. The shared tau pathway that can be activated by TBI (shown here), AD, and FTDP-17 (20, 21) unravels a neurobiological basis for the high risks of AD in boxers, football players, and military personnel (6–10). Our characterization of mechanical components associated with neuronal injuries may provide information for future development of protective gear for soldiers and athletes and a starting point for development of therapeutic strategies to target the signaling pathways involved in tau-mediated synaptic dysfunction to treat and prevent CTE.

Methods

Sulcus and Microvessel Models. Mechanical deformation in the sulcus and microvessel-surrounding tissue were simulated using COMSOL Multiphysics 4.2. Both were modeled as 2D plane strain bodies with linear elastic material properties, undergoing quasi-static deformation. In both models, brain tissue was treated as an isotropic linear elastic material given by

$$\sigma_{ij} = 2\mu\epsilon_{ij} + \lambda\delta_{ij}\sum_{k=1}^3\epsilon_{kk}, \quad [1]$$

where σ_{ij} and ϵ_{ij} are the i, j components of the stress and strain tensors, respectively; δ_{ij} is a Kronecker delta; μ is the shear modulus; and λ is the first

Lamé parameter. These material properties can be given in terms of the more common Young's modulus (E) and Poisson's ratio (ν) by

$$\mu = \frac{E}{\nu(1+\nu)}, \lambda = \frac{E\nu}{(1+\nu)(1-2\nu)}. \quad [2]$$

The material parameters were estimated based on previous studies (65) as $E = 1.895\text{kPa}$ and $\nu = 0.45$. In the microvessel model, the vessel wall was also treated as a linear elastic material, with a Young's modulus given as $E_{\text{vessel}} = \alpha E_{\text{brain}}$, where α is a scalar where $\alpha \geq 1$, and $\nu = 0.45$.

In the sulcus model, roller boundary conditions were applied to the side and bottom edges of the brain tissue section, and a contact pair was created between the rigid indenter and the sulcal boundary of brain tissue. Incremental displacements were prescribed to the indenter, which in turn initiated the contact between indenter and brain tissue. The volume of the intrasulcal space was not conserved, as the cerebrospinal fluid found in the sulci, in vivo, is free to flow out of the sulci and about the intracranial space. In the microvessel model, a roller boundary condition was used on the bottom boundary, and the top boundary was uniformly displaced. To model incompressible blood within the vessel, the volume of the lumen was conserved.

The geometry of the model was meshed with triangular elements, and the parametric solver was used to determine the effects of geometry and material properties on model behavior. Parameters that were tested were the sulcal depth, sulcal width, gyral radius, sulcal radius, microvessel diameter, microvessel wall thickness, and microvessel stiffness ratio (α). In all models, the first principal strain, defined as the largest eigenvalue of the strain tensor, was calculated, and the peak values within the brain tissue during deformation were reported.

Stretching Construct Preparation. High-velocity stretching constructs were prepared for cell culture by first spin-coating 0.010" thick silicone sheeting (SMI) with a 10- μm -thick layer of Sylgard 527 PDMS (Ellsworth Adhesives) at a 1:1 base to crosslinker ratio. After curing, these membranes were suspended under tension between two custom-designed metal brackets (Oakdale Precision), and a Sylgard 184 PDMS (Ellsworth Adhesives) ring was adhered to the membrane to contain cell culture media upon cell seeding. The constructs were treated with a UVO-Cleaner (Jelight Co. Inc.) for 8 min

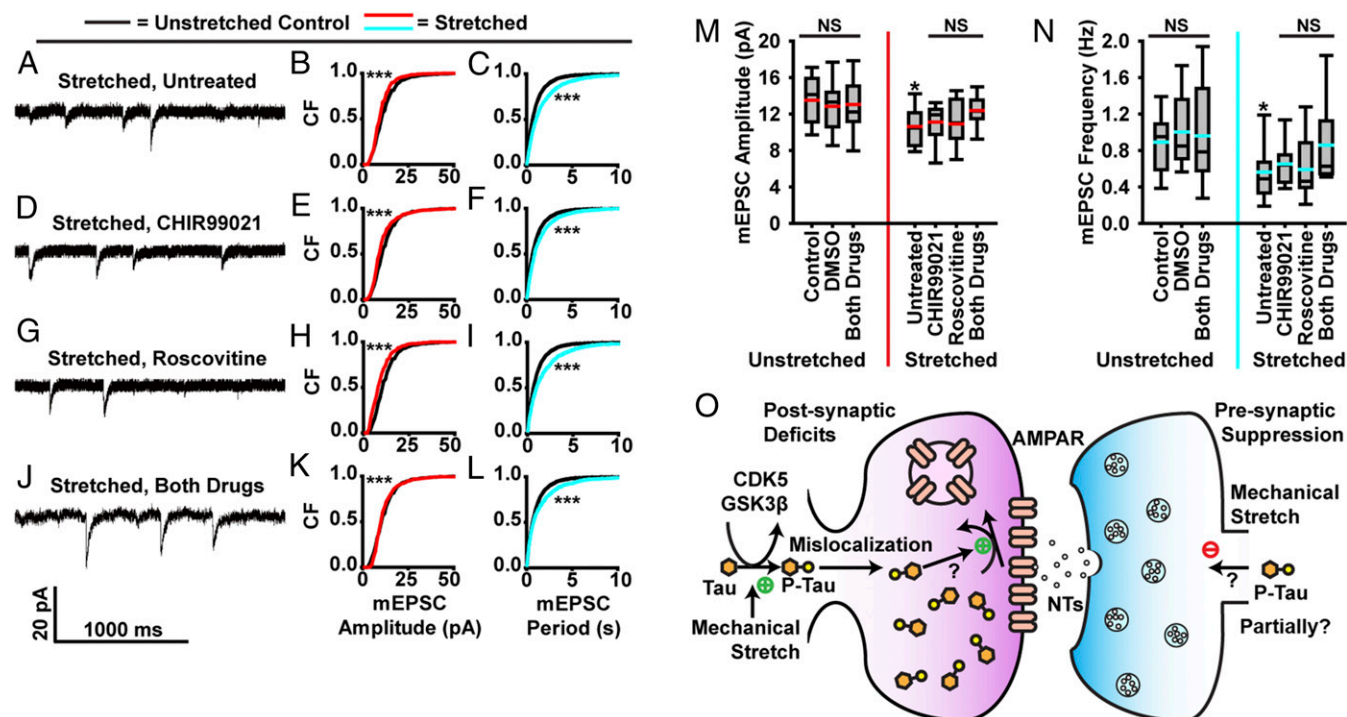


Fig. 7. Stretch-induced tau mislocalization and hyperphosphorylation mediate synaptic dysfunction. (A–L) Effect of GSK3 β and CDK5 inhibition on mEPSC dynamics. A, D, G, and J are representative mEPSC recordings from neurons exposed to stretch. B, E, H, and K show cumulative frequency of mEPSC amplitudes (black, unstretched control; red, stretched and treated; bins, 1 pA). C, F, I, and L show cumulative frequency of mEPSC peak-to-peak period (black, unstretched control; teal, stretched and treated; bins, 50 ms). (A–C) Untreated. (D–F) Pretreated with 500 nM CHIR99021 to inhibit GSK3 β . (G–I) Pretreated with 500 nM Roscovitine to inhibit CDK5. (J–L) Pretreated with both CHIR99021 and Roscovitine. (M) Quantification of mEPSC amplitudes (black line, median; red line, mean; box, 25 to 75%; whisker, 10 to 90%). (N) mEPSC frequency (black line, median; teal, mean; box, 25 to 75%; whisker, 10 to 90%). (O) Proposed molecular framework of the postsynaptic deficits and presynaptic suppression caused by mechanical injury. While most postsynaptic deficits depend upon tau, other factors independent upon tau may contribute to presynaptic deficits. For cumulative frequency distribution plots, K-S tests were used to compare treated and/or stretched groups to unstretched–untreated controls. D/D_{crit}: B, 4.31; C, 5.48; E, 4.79; F, 3.33; H, 5.11; I, 4.30; K, 1.82; L, 2.98; $\alpha = 0.05$ for all. Cells/mEPSCs: control, 18/4,360; DMSO, 13/1,464; unstretched–both drugs, 11/1,571; stretched–untreated, 23/3,139; CHIR99021, 10/2,481; Roscovitine, 11/1,352; stretched–both drugs, 14/1,255. In all plots, * $P < 0.05$, *** $P < 0.001$ compared to control, and NS is not significant. Note that K-S test significance in K is due to variations in low-amplitude events, not a difference in the means (M). Were these small events (<7 pA) excluded, the treated and control groups would not be significantly different. The two curves in K are obviously much closer than those in B, E, and H; nevertheless, it is possible that the highly sensitive nonparametric K-S test can still detect some residual effects of TBI.

and then incubated in a solution of 100 μ g/mL poly-D-lysine and 4 μ g/mL laminin (Sigma-Aldrich) in a cell culture incubator overnight.

Cell Isolation and Culture. Primary hippocampal neurons were harvested from Hsd:Sprague–Dawley newborn rat pups as previously described (Envigo) (66). Hippocampi from each pup were isolated and pooled together in ice-cold Earl's Balanced Medium supplemented with 1 mM D-glucose before tissues were digested, meaning that hippocampal neurons from each pup were combined and mixed with hippocampal neurons from its littermates. Cells were then seeded onto the stretching constructs at a density of 10^6 cells per construct in plating media (minimal essential media with Earle's salts, 10 mM Hepes, 10 mM sodium pyruvate, 0.5 mM glutamine, 12.5 μ M glutamate, 10% FBS, and 0.6% glucose) (Thermo Fisher Scientific). The day of plating was denoted as day-in-vitro 1 or DIV1. Approximately 4 h after plating, the media was replaced with fresh plating media to remove nonadherent cells and debris. Twenty-four hours after plating, media was replaced with NbActiv1 neuron culture medium media (BrainBits, LLC). Cells were maintained in a 37 $^{\circ}$ C, 5% CO $_2$ environment throughout the duration of the experiment. Fifty percent media changes with NbActiv1 were performed on a weekly basis. For mouse experiments, the same cell isolation and culture protocols were followed. C57BL/6J mice (TgNg) and B6.129 \times 1-Mapt^{tm1Hnd/J} mice (Tau-KO) were used (Jackson Laboratory).

Simulated TBI via High-Strain Rate Stretching. To simulate the mechanical deformations in the brain during a TBI we applied a high-strain rate acute uniaxial stretch to cultured hippocampal neurons at DIV 22. A linear motor (PS01-23 \times 80F/100 \times 160-HP-R, LinMot USA) was used to displace one end of the cell-seeded elastic substrate with fine control over both strain (ϵ) and

strain rate ($\dot{\epsilon}$), to simulate injury. Single stretches were performed with $\epsilon = 0$ to 20% and $\dot{\epsilon} = 0$ to 1,000%/s. For repeated stretch experiments, stretches of $\epsilon = 2\%$ and $\dot{\epsilon} = 1,000\%/s$ were applied in 1-s intervals 1, 5, 10, or 20 times.

Transfection Constructs. Each of the human-tau constructs was tagged with enhanced GFP (denoted as GFP) on the N terminus, expressed in the pRK5 vector, and driven by a cytomegalovirus (CMV) promoter (Clontech, Inc.). The DsRed constructs (Clontech, Inc.) were also expressed in the pRK5 vector and driven by a CMV promoter. The WT-tau construct encoded human 4R tau lacking the N-terminal sequences (4R0N) and contained exons 1, 4 to 5, 7, and 9 to 13; intron 13; and exon 14. WT-tau was used as a template to create an AP tau construct, which was generated by mutating all 14 S/P or T/P amino acid residues (T111, T153, T175, T181, S199, S202, T205, T212, T217, T231, S235, S396, S404, and S422; numbering based on the longest 441-amino acid brain isoform of tau) to alanine. The PCR-mediated site-directed mutagenesis was confirmed by sequencing.

Transfection and Imaging. A standard calcium phosphate precipitation method was used to transfect hippocampal neurons with desired plasmids at DIV7–8 (67). Neurons were cotransfected with DsRed and either httau variant (WT or AP) at a 2:1 ratio. DsRed was used to visualize the morphology of neurons, including the location of dendritic spines. Transfected cells were then allowed to mature for 2 wk before further experimentation. Twenty-four hours after stretch was applied, the constructs were mounted to a platform above a Nikon inverted epifluorescent microscope using a custom-designed stage attachment. All images of neurons transfected with DsRed and WT-tau or AP tau were acquired using a 40 \times water immersion lens and

computerized focus motor starting at DIV 23. All digital images were acquired using MetaMorph Imaging System (Universal Imaging Corporation) as 15-image stacks with a 0.5- μm step in the Z direction separating each image. Stacks were processed via MetaMorph Imaging System's 2D nearest neighbors deconvolution function before removing out-of-focus slices and averaging the stack into a single image. DsRed and WT- or AP tau images were paired and overlaid in Adobe Photoshop (Adobe Inc.) in order to count dendritic spines and the presence or lack of tau in each dendritic spine. Each dendritic spine was treated as a binary event (tau present or no tau present), and the total sample population of dendritic spines was used for statistical analysis. For spine density counts, two dendrites were traced in their entirety for each acquired image, and the length was recorded in microns. Dendritic spines were counted along each dendrite, and dendritic spines per 100 microns were calculated for each image, using the image average value for statistical analysis. The ratio of DsRed fluorescent intensity to GFP fluorescent intensity was calculated and recorded for each image to ensure that no results owed to erroneous fluctuations in the transfection efficiency of either plasmid. For each acquired image, the brightness of DsRed and GFP were recorded at three neural processes and then averaged. Each of these averages was used to compute group means and SDs. A maximum of two cells per dish were imaged for tau mislocalization imaging experiments.

Electrophysiology. Miniature EPSCs were recorded from hippocampal neurons at DIV 23 using 5 megaohm glass pipettes at holding potential of -55 mV (20). Recording in whole-cell configuration lasted up to 5 min, using an Axopatch 200B amplifier and pClamp 11 (Molecular Devices). For each second, one recording sweep of 200 ms was sampled. Recordings were filtered at 1 kHz with an output gain of $\alpha = 1$. Neurons were rinsed once with artificial cerebrospinal fluid (ACSF) at room temperature containing 100 μM APV (an NMDAR antagonist), 1 μM TTX (a sodium channel blocker), and 100 μM picrotoxin (GABA_A receptor antagonist) and then bathed in ACSF for electrophysiology while being gassed with 95% O_2 –5% CO_2 . ACSF was composed of 119 mM NaCl, 2.5 mM KCl, 5.0 mM CaCl_2 , 2.5 mM MgCl_2 , 26.2 mM NaHCO_3 , 1 mM NaH_2PO_4 , and 11 mM glucose. The patch pipette was filled with an internal solution containing 100 mM cesium gluconate, 0.2 mM EGTA, 0.5 mM MgCl_2 , 2 mM ATP, 0.3 mM GTP, and 40 mM Hepes (pH 7.2 with CsOH) (Sigma-Aldrich). All mEPSCs were manually identified with the MiniAnalysis software (Synaptosoft Inc.) based on a threshold amplitude of 3 pA, a characteristic fast-rising phase, and a slow-decaying phase. The amplitude and frequency of all recorded and verified mEPSCs were averaged for each neuron and treated as a single sample for further statistical analysis. A maximum of one cell per dish was patched for all electrophysiology experiments.

Inhibition of Tau Hyperphosphorylation. Using DMSO (Sigma-Aldrich), 1,000 \times (500 mM) solutions of CHIR99021 and Roscovitine (Sigma-Aldrich) were made. The 1,000 \times solutions were mixed with cell media to create a 1 \times (500 nM) solution. Neurons were treated with CHIR99021, Roscovitine, or both drugs 1 h before stretching, and the media containing drugs was left on the neurons throughout the remaining duration of experiments.

Immunocytochemistry. Cultured neurons were fixed and permeabilized with 4% paraformaldehyde + 4% sucrose (23 $^{\circ}\text{C}$, 30 min), 100% methanol (-20 $^{\circ}\text{C}$ at the beginning, incubated at 23 $^{\circ}\text{C}$ for 20 min), and 0.2% Triton X-100 (23 $^{\circ}\text{C}$, 20 min) applied successively as previously described (20). For all immunocytochemical staining, both primary and secondary antibodies were diluted at 1:100 in 10% donkey serum in PBS. The fixed neurons were incubated with primary antibodies at room temperature overnight and subsequently incubated with rhodamine (red)- or FITC (green)-labeled secondary antibodies for 1.5 h at room temperature. The stained cultures were mounted with a 0.8-mm-thick coverslip with Permafluor Aqueous Mounting Medium (TA-030-FM, Thermo Fisher) and imaged with a Nikon microscope with a 63 \times oil objective. In *SI Appendix, Fig. S3*, neurons expressing GFP-tagged wild-type human tau proteins were incubated with a primary mouse monoclonal anti-Synaptophysin antibody (MAB5258; from Millipore) and subsequently with a goat rhodamine (red)-linked secondary anti-mouse antibody to detect presynaptic terminals. Putative functional dendritic spines were defined as GFP-labeled mushroom-like structures (green) that are colocalized with or adjacent to a presynaptic terminal labeled by the anti-Synaptophysin antibody (red). In *SI Appendix, Fig. S4*, cultures were coincubated with the widely used mouse monoclonal anti-tau antibody Tau-5 (sc-58860; Santa Cruz Biotechnology) and a rabbit polyclonal anti-synaptophysin antibody (RP036; from Diagnostic Biosystems); they were subsequently incubated with a goat secondary FITC (green)-linked anti-mouse antibody and a goat secondary Rhodamine (red)-linked anti-rabbit

antibody to detect endogenous tau and presynaptic terminals, respectively. For Synaptophysin cluster density counts, two neurites were traced in their entirety for each acquired image, and the length was recorded in microns. Synaptophysin clusters were counted along each neurite, and clusters per 100 microns were calculated for each image, using the image average value for statistical analysis.

Viscoelastic Neuron Model. Mechanical energy added to the dendritic spine during injury was determined by calculating the work per unit volume done on the cell during stretching. Neurons have previously been shown to act as viscoelastic Kelvin solids (45), but neurites are significantly more fluid-like than the soma and become more fluidic with increasing stress (46). To capture both of these observations, we modeled the neurite as a standard viscoelastic solid with two springs and one dashpot (Fig. 3G) and described by the equation

$$\frac{\dot{\sigma}}{E_1} + \frac{\sigma}{\eta_1} = \frac{E_1 + E_2}{E_1} \dot{\epsilon} + \frac{E_2}{\eta_1} \epsilon, \quad [3]$$

where σ is the stress; ϵ is the strain; $\dot{\sigma}$ and $\dot{\epsilon}$ are the stress and strain rates, respectively; E_1 and E_2 are the moduli of the springs; and η_1 is the viscosity of the dashpot. E_1 , E_2 , and η_1 were determined by simulating a creep test, as performed by Grevesse et al. (46), and fitting the parameters to their results using least squares fitting.

To model neurite stretching, we let ϵ and $\dot{\epsilon}$ match those applied experimentally (Fig. 3H) and calculated σ using Eq. 3 and finite differences. The work per unit volume (w) was taken as

$$w = \int \sigma d\epsilon \quad [4]$$

over the period from the initiation of stretch to the time at which ϵ is at its peak value. For repeated stretch analyses, the total work was taken as the sum of the work of each stretch.

A parameter study was performed to determine how the values of E_1 , E_2 , and η_1 influence the results by setting $E_1 = \beta E_2$ and repeating the solution above for a given β (*SI Appendix, Fig. S8*).

Statistical Analyses and Reproducibility. In the case of quantifying tau mislocalization, a total number of dendritic spines and dendritic spines containing an observable tau presence (summed from all recorded images) was documented for each experimental treatment. From this, a proportion of dendritic spines containing tau was calculated for each experimental group. A χ^2 test for multiple proportions was performed to assess whether statistical differences existed between all groups, and then two-proportion pooled z tests were performed pairwise to determine which groups were statistically different from one another. For dendritic spine density electrophysiology, synaptophysin cluster density, and tau/synaptophysin colocalization data, one-way ANOVA was performed to test for variance between all groups, followed by a post hoc Tukey test for pairwise comparisons. For cumulative frequency distributions, K-S tests were used to compare mEPSC amplitude and period distributions between unstretched controls and all treated groups. The ratio of the K-S test statistic (D) to the statistical critical value (D_{crit}) is presented in the appropriate figure caption. All tests had statistical significance set for $\alpha = 0.05$. χ^2 tests, two-proportion pooled z tests, ANOVA, and Tukey tests were performed using SigmaPlot 11.0 (Systat Software Inc.). K-S tests were performed using Microsoft Excel (Microsoft).

In total, tau mislocalization experiments utilized 25 different litters of rat pups, with an approximate litter size of 10 to 12 pups. Cells from each of these litters were transfected to assess tau mislocalization or to confirm colocalization of tau and Synaptophysin. Electrophysiology experiments required 17 litters of rat pups. For both experiments, each litter came from a different timed-pregnancy rat dam, which was euthanized after giving birth. TgNg and Tau-KO mouse pups for electrophysiology experiments were bred by us. Two males and four females of each genotype were purchased, and three litters of each genotype were used for experiments. Each litter of pups had a distinct parentage to maintain genetic diversity variation within the experiment.

Animal Usage. The breeding, handling and usage of rats and mice have been approved by the Institutional Animal Care and Use Committee (IACUC) at the University of Minnesota (Protocol #1809-36344A). Rat and mouse pups (< 1 week old) were decapitated to harvest brain tissues strictly following the IACUC guidelines.

Data Availability. All study data are included in the article and *SI Appendix*.

ACKNOWLEDGMENTS. We thank Peter Teravskis for his technical expertise and thoughtful discussions. Funding was provided by NIH Grants R21-NS096437-01 (D.L. and P.W.A.) and R61 NS115089-01 (D.L.), Minnesota Higher Education Grant (D.L. and P.W.A.), Institute of Engineering Medicine

at the University of Minnesota (UMN) seed grant (P.W.A. and D.L.), UMN–Mayo Partnership Grant (D.L.), and NSF Grants Civil, Mechanical and Manufacturing Innovation (CMMI) 1553255 (P.W.A.) and CMMI 1935834 (P.W.A. and D.L.).

1. C. A. Taylor, J. M. Bell, M. J. Breiding, L. Xu, Traumatic brain injury-related emergency department visits, hospitalizations, and deaths—United States, 2007 and 2013. *MMWR Surveill. Summ.* **66**, 1–16 (2017).
2. J. A. Langlois, W. Rutland-Brown, M. M. Wald, The epidemiology and impact of traumatic brain injury: A brief overview. *J. Head Trauma Rehabil.* **21**, 375–378 (2006).
3. B. Roozenbeek, A. I. R. Maas, D. K. Menon, Changing patterns in the epidemiology of traumatic brain injury. *Nat. Rev. Neurol.* **9**, 231–236 (2013).
4. B. I. Omalu et al., Chronic traumatic encephalopathy in a National Football League player. *Neurosurgery* **57**, 128–134, discussion 128–134 (2005).
5. B. I. Omalu et al., Chronic traumatic encephalopathy in a National Football League player: Part II. *Neurosurgery* **59**, 1086–1092, discussion 1092–1093 (2006).
6. B. I. Omalu, J. Bailes, J. L. Hammers, R. P. Fitzsimmons, Chronic traumatic encephalopathy, suicides and parasuicides in professional American athletes: The role of the forensic pathologist. *Am. J. Forensic Med. Pathol.* **31**, 130–132 (2010).
7. A. C. McKee et al., The spectrum of disease in chronic traumatic encephalopathy. *Brain* **136**, 43–64 (2013).
8. B. E. Gavett, R. A. Stern, A. C. McKee, Chronic traumatic encephalopathy: A potential late effect of sport-related concussive and subconcussive head trauma. *Clin. Sports Med.* **30**, 179–188, xi (2011).
9. A. C. McKee, M. E. Robinson, Military-related traumatic brain injury and neurodegeneration. *Alzheimers Dement.* **10**, S242–S253 (2014).
10. B. L. Plassman et al., Documented head injury in early adulthood and risk of Alzheimer's disease and other dementias. *Neurology* **55**, 1158–1166 (2000).
11. S. Fleminger, D. L. Oliver, S. Lovestone, S. Rabe-Hesketh, A. Giora, Head injury as a risk factor for Alzheimer's disease: The evidence 10 years on; a partial replication. *J. Neurol. Neurosurg. Psychiatry* **74**, 857–862 (2003).
12. J. H. Bower et al., Head trauma preceding PD: A case-control study. *Neurology* **60**, 1610–1615 (2003).
13. P. N. Nemetz et al., Traumatic brain injury and time to onset of Alzheimer's disease: A population-based study. *Am. J. Epidemiol.* **149**, 32–40 (1999).
14. A. Jawaid, R. Rademakers, J. S. Kass, Y. Kalkonde, P. E. Schulz, Traumatic brain injury may increase the risk for frontotemporal dementia through reduced progranulin. *Neurodegener. Dis.* **6**, 219–220 (2009).
15. F. P. Chong, K. Y. Ng, R. Y. Koh, S. M. Chye, Tau proteins and tauopathies in Alzheimer's disease. *Cell. Mol. Neurobiol.* **38**, 965–980 (2018).
16. C. Conde, A. Cáceres, Microtubule assembly, organization and dynamics in axons and dendrites. *Nat. Rev. Neurosci.* **10**, 319–332 (2009).
17. J. Chen, Y. Kanai, N. J. Cowan, N. Hirokawa, Projection domains of MAP2 and tau determine spacings between microtubules in dendrites and axons. *Nature* **360**, 674–677 (1992).
18. N. M. Kanaan et al., Pathogenic forms of tau inhibit kinesin-dependent axonal transport through a mechanism involving activation of axonal phosphotransferases. *J. Neurosci.* **31**, 9858–9868 (2011).
19. L. Zhou et al., Tau association with synaptic vesicles causes presynaptic dysfunction. *Nat. Commun.* **8**, 15295 (2017).
20. B. R. Hoover et al., Tau mislocalization to dendritic spines mediates synaptic dysfunction independently of neurodegeneration. *Neuron* **68**, 1067–1081 (2010).
21. E. C. Miller et al., Tau phosphorylation and tau mislocalization mediate soluble A β oligomer-induced AMPA glutamate receptor signaling deficits. *Eur. J. Neurosci.* **39**, 1214–1224 (2014).
22. D. Liao, E. C. Miller, P. J. Teravskis, Tau acts as a mediator for Alzheimer's disease-related synaptic deficits. *Eur. J. Neurosci.* **39**, 1202–1213 (2014).
23. P. J. Teravskis et al., Phosphorylation in two discrete tau domains regulates a stepwise process leading to postsynaptic dysfunction. *J. Physiol.*, 10.1113/JP277459 (2019).
24. P. J. Teravskis, K. H. Ashe, D. Liao, The accumulation of tau in postsynaptic structures: A common feature in multiple neurodegenerative diseases? *Neuroscientist* **26**, 503–520 (2020).
25. E. Kim, K. Sakata, F. F. Liao, Bidirectional interplay of HSF1 degradation and UPR activation promotes tau hyperphosphorylation. *PLoS Genet.* **13**, e1006849 (2017).
26. X. Zhao et al., Caspase-2 cleavage of tau reversibly impairs memory. *Nat. Med.* **22**, 1268–1276 (2016).
27. S. W. Min et al., Acetylation of tau inhibits its degradation and contributes to tauopathy. *Neuron* **67**, 953–966 (2010).
28. T. E. Tracy et al., Acetylated tau obstructs KIBRA-mediated signaling in synaptic plasticity and promotes tauopathy-related memory loss. *Neuron* **90**, 245–260 (2016).
29. V. M.-Y. Lee, M. Goedert, J. Q. Trojanowski, Neurodegenerative tauopathies. *Annu. Rev. Neurosci.* **24**, 1121–1159 (2001).
30. A. C. McKee et al., Chronic traumatic encephalopathy in athletes: Progressive tauopathy after repetitive head injury. *J. Neuropathol. Exp. Neurol.* **68**, 709–735 (2009).
31. A. C. McKee, T. D. Stein, P. T. Kiernan, V. E. Alvarez, The neuropathology of chronic traumatic encephalopathy. *Brain Pathol.* **25**, 350–364 (2015).
32. A. C. McKee, D. H. Daneshvar, "The neuropathology of traumatic brain injury" in *Handbook of Clinical Neurology*, J. Grafman, A. M. Salazar, Eds. (Elsevier, 2015), Vol. 127, pp. 45–66.
33. P. H. Montenegro, D. T. Corp, T. D. Stein, R. C. Cantu, R. A. Stern, Chronic traumatic encephalopathy: Historical origins and current perspective. *Annu. Rev. Clin. Psychol.* **11**, 309–330 (2015).
34. M. Ghajari, P. J. Hellyer, D. J. Sharp, Computational modelling of traumatic brain injury predicts the location of chronic traumatic encephalopathy pathology. *Brain* **140**, 333–343 (2017).
35. M. A. Hemphill et al., A possible role for integrin signaling in diffuse axonal injury. *PLoS One* **6**, e22899 (2011).
36. P. W. Alford et al., Blast-induced phenotypic switching in cerebral vasospasm. *Proc. Natl. Acad. Sci. U.S.A.* **108**, 12705–12710 (2011).
37. P. V. Bayly, E. E. Black, R. C. Pedersen, E. P. Leister, G. M. Genin, In vivo imaging of rapid deformation and strain in an animal model of traumatic brain injury. *J. Biomech.* **39**, 1086–1095 (2006).
38. J. Zhang, Y. Yang, H. Li, J. Cao, L. Xu, Amplitude/frequency of spontaneous mEPSC correlates to the degree of long-term depression in the CA1 region of the hippocampal slice. *Brain Res.* **1050**, 110–117 (2005).
39. H.-K. Lee, K. Kameyama, R. L. Huganir, M. F. Bear, NMDA induces long-term synaptic depression and dephosphorylation of the GluR1 subunit of AMPA receptors in hippocampus. *Neuron* **21**, 1151–1162 (1998).
40. B. A. Earnshaw, P. C. Bressloff, Biophysical model of AMPA receptor trafficking and its regulation during long-term potentiation/long-term depression. *J. Neurosci.* **26**, 12362–12373 (2006).
41. R. Schneggenburger, C. Rosenmund, Molecular mechanisms governing Ca(2+) regulation of evoked and spontaneous release. *Nat. Neurosci.* **18**, 935–941 (2015).
42. Y. Feng, E. H. Clayton, Y. Chang, R. J. Okamoto, P. V. Bayly, Viscoelastic properties of the ferret brain measured in vivo at multiple frequencies by magnetic resonance elastography. *J. Biomech.* **46**, 863–870 (2013).
43. E. H. Clayton, J. R. Garbow, P. V. Bayly, Frequency-dependent viscoelastic parameters of mouse brain tissue estimated by MR elastography. *Phys. Med. Biol.* **56**, 2391–2406 (2011).
44. S. Budday, G. Sommer, G. A. Holzapfel, P. Steinmann, E. Kuhl, Viscoelastic parameter identification of human brain tissue. *J. Mech. Behav. Biomed. Mater.* **74**, 463–476 (2017).
45. Y.-B. Lu et al., Viscoelastic properties of individual glial cells and neurons in the CNS. *Proc. Natl. Acad. Sci. U.S.A.* **103**, 17759–17764 (2006).
46. T. Gresses, B. E. Dabiri, K. K. Parker, S. Gabriele, Opposite rheological properties of neuronal microcompartments predict axonal vulnerability in brain injury. *Sci. Rep.* **5**, 9475 (2015).
47. S. Jayapalan, J. Natarajan, The role of CDK5 and GSK3B kinases in hyperphosphorylation of microtubule associated protein tau (MAPT) in Alzheimer's disease. *Bioinformation* **9**, 1023–1030 (2013).
48. B. P. Lucke-Wold et al., Linking traumatic brain injury to chronic traumatic encephalopathy: Identification of potential mechanisms leading to neurofibrillary tangle development. *J. Neurotrauma* **31**, 1129–1138 (2014).
49. B. Morrison 3rd, B. S. Elkin, J.-P. Dollé, M. L. Yarmush, In vitro models of traumatic brain injury. *Annu. Rev. Biomed. Eng.* **13**, 91–126 (2011).
50. E. W. Vogel 3rd, S. H. Rwema, D. F. Meaney, C. R. Bass, B. Morrison 3rd, Primary blast injury depressed hippocampal long-term potentiation through disruption of synaptic proteins. *J. Neurotrauma* **34**, 1063–1073 (2017).
51. N. J. Brown et al., Effect of cognitive activity level on duration of post-concussion symptoms. *Pediatrics* **133**, e299–e304 (2014).
52. J. Yang, C. Peek-Asa, T. Covassin, J. C. Torner, Post-concussion symptoms of depression and anxiety in division I collegiate athletes. *Dev. Neuropsychol.* **40**, 18–23 (2015).
53. P. H. Montenegro, C. Bernick, R. C. Cantu, Clinical features of repetitive traumatic brain injury and chronic traumatic encephalopathy. *Brain Pathol.* **25**, 304–317 (2015).
54. D. F. Meaney, B. Morrison, C. Dale Bass, The mechanics of traumatic brain injury: A review of what we know and what we need to know for reducing its societal burden. *J. Biomech. Eng.* **136**, 021008 (2014).
55. J. M. Meythaler, J. D. Peduzzi, E. Eleftheriou, T. A. Novack, Current concepts: Diffuse axonal injury-associated traumatic brain injury. *Arch. Phys. Med. Rehabil.* **82**, 1461–1471 (2001).

56. H. Ahmadzadeh, D. H. Smith, V. B. Shenoy, Viscoelasticity of tau proteins leads to strain rate-dependent breaking of microtubules during axonal stretch injury: Predictions from a mathematical model. *Biophys. J.* **106**, 1123–1133 (2014).
57. H. Song *et al.*, Linking blast physics to biological outcomes in mild traumatic brain injury: Narrative review and preliminary report of an open-field blast model. *Behav. Brain Res.* **340**, 147–158 (2018).
58. Y. Chen, S. Constantini, Caveats for using shock tube in blast-induced traumatic brain injury research. *Front. Neurol.* **4**, 117 (2013).
59. J. Del Castillo, B. Katz, Quantal components of the end-plate potential. *J. Physiol.* **124**, 560–573 (1954).
60. D. Liao, N. A. Hessler, R. Malinow, Activation of postsynaptically silent synapses during pairing-induced LTP in CA1 region of hippocampal slice. *Nature* **375**, 400–404 (1995).
61. J. F. Abisambra, S. Scheff, Brain injury in the context of tauopathies. *J. Alzheimers Dis.* **40**, 495–518 (2014).
62. Y. Okada, H. Yamazaki, Y. Sekine-Aizawa, N. Hirokawa, The neuron-specific kinesin superfamily protein KIF1A is a unique monomeric motor for anterograde axonal transport of synaptic vesicle precursors. *Cell* **81**, 769–780 (1995).
63. P. Guedes-Dias, E. L. F. Holzbaur, Axonal transport: Driving synaptic function. *Science* **366**, eaaw9997 (2019).
64. M. D. Tang-Schomer, V. E. Johnson, P. W. Baas, W. Stewart, D. H. Smith, Partial interruption of axonal transport due to microtubule breakage accounts for the formation of periodic varicosities after traumatic axonal injury. *Exp. Neurol.* **233**, 364–372 (2012).
65. S. Budday *et al.*, Mechanical properties of gray and white matter brain tissue by indentation. *J. Mech. Behav. Biomed. Mater.* **46**, 318–330 (2015).
66. H. Lin, R. Huganir, D. Liao, Temporal dynamics of NMDA receptor-induced changes in spine morphology and AMPA receptor recruitment to spines. *Biochem. Biophys. Res. Commun.* **316**, 501–511 (2004).
67. R. E. Kingston, C. A. Chen, J. K. Rose, Calcium phosphate transfection. *Curr. Protoc. Mol. Biol.* **63**, 9.1.1–9.1.11 (2003).